Nongravitational Effects of Cometary Activity

Stefano Mottola[1] · **Nicholas Attree[2]** · **Laurent Jorda[3]** ·
Horst Uwe Keller[4,1] · **Rosita Kokotanekova[5]** ·
David Marshall[6] · **Yuri Skorov[4]**

Abstract Nongravitational forces induced by sublimation of volatiles affect the rotational and orbital dynamics of comets. In addition to contributing to the improvement of ephemerides and of rotational models, nongravitational effects can help constrain the regional distribution and temporal evolution of cometary activity, which in turn provides input for the development of thermophysical and dust transport models. We review the progress that has been made in this field thanks to the Rosetta mission and we highlight the open questions.

Keywords Nongravitational acceleration · Orbital evolution · Cometary activity

1 Introduction

The very defining property of comets—the one that sets comets apart from other minor bodies—is the occurrence of gradual sublimation of their icy components under the influ-

✉ S. Mottola
stefano.mottola@dlr.de

1   Institute of Planetary Research, DLR, Rutherfordstrasse 2, 12489 Berlin, Germany

2   Earth and Planetary Observation Centre, Dept. of Biological and Environmental Sciences, University of Stirling, Stirling, UK

3   Laboratoire d'Astrophysique de Marseille, Aix Marseille Univ., CNRS, CNES, 13388 Marseille Cedex 13, France

4   Institute for Geophysics and Extraterrestrial Physics, TU Braunschweig, 38106 Braunschweig, Germany

5   European Southern Observatory (ESO), Karl-Schwarzschild Str. 2, 85748 Garching bei München, Germany

6   Max-Planck-Institut für Sonnensystemforschung, Justus-von-Liebig-Weg, 3, 37077 Göttingen, Germany

ence of solar irradiation. Sublimation results in the release of gas and debris (ranging in size from sub-µm to several meters, and often collectively called cometary dust) that form the comet's coma and tail. The complex manifestations that accompany sublimation, and that are generally referred to as cometary activity, have a profound influence on the comet evolution, contributing to sculpt and re-organize its shape, change its mass, modify its orbit and rotation state, and possibly lead it to its disintegration.

By studying the effects of activity it is possible to infer the physical as well as both rotational and orbital dynamical properties of a comet, to put independent constraints on the production rates of the dust and of different volatile species, and to map the distribution of the source regions on the surface.

In this paper we concentrate on the measurable effects of activity on the orbital and rotational dynamics of comets. These effects, which have been recognized and studied for two centuries, have now been measured with unprecedented accuracy for comet 67P/Churyumov-Gerasimenko (hereafter 67P) during the Rosetta mission.

1.1 Orbital Dynamics

The recoil forces from activity induce a nongravitational acceleration (NGA) that produces measurable deviations from a pure Keplerian orbit. Such an effect was first noticed for 2P/Encke (Enke 1823), although it was Bessel (1835) who first recognized the reaction by ejected material as a possible cause. The first interest in NGAs resulted therefore from the necessity of accurately describing the orbit of a comet for the purpose of recovering it during subsequent apparitions. Marsden (1969) laid out the problem—in what is now known as the standard model—by defining a nongravitational acceleration term that is summed to the Keplerian acceleration, and that is assumed to be proportional to an *activity function* $g(r)$. The latter is an empirical function seeking to describe the variation of the vaporization flux of water ice (which is the dominant volatile species) as a function of the heliocentric distance (Marsden et al. 1973). The NGA is decomposed into three orthogonal components defined in the orbit-plane reference system—the radial, transverse and normal component. The nongravitational acceleration A_{ng} can therefore be expressed as:

$$A_{ng} = g(r)(A_1 R + A_2 T + A_3 N) \tag{1}$$

where r is the heliocentric range and R, T, and N are the radial, transverse and normal unit vectors. For the purpose of orbit determination, the quantities A_i are, in general, considered constant and derived as a fit to the astrometric data. This procedure generally produces results that are in very good agreement with the astrometric data, and certainly within the errors of ground-based measurements. Equation (1), however, is a crude simplification of the physics of cometary activity, especially in the assumption that the A_i coefficients are constant over the comet's orbit. For this reason, the A_i quantities are suitable as fitting parameters, but the corresponding nongravitational acceleration A_{ng} may considerably differ from the actual nongravitational acceleration at any given time (Yeomans et al. 2004).

Rickman (1986) showed that by integrating the Gauss' equation one could express the variation of the orbital period ΔP as a function of the NGA in the form:

$$\Delta P = 6\pi \frac{\sqrt{1-e^2}}{n^2} \left(\frac{e}{q(1+e)} \int_0^P A_1 g(r) \sin \nu \, dt + \int_0^P A_2 \frac{g(r)}{r} \, dt \right) \tag{2}$$

where P is the orbital period, e is the eccentricity, q is the perihelion distance, ν is the true anomaly, and n is the mean motion. If the A_i quantities are strictly constant over the

orbit, then the integral of the radial acceleration component is zero, and the variation of the orbital period only depends on the transverse component A_2. Although it is known that many comets show a significant activity asymmetry with respect to perihelion—which implies that the A_i quantities are *not* constant—the study of A_2 still provides some physical information, at least in a statistical sense. Rickman et al. (1991), for example, have correlated the A_2 parameter to the evolutionary age in a sample of short-period comets.

A more sophisticated approach seeks to determine the nongravitational force vector as a function of the heliocentric distance by estimating the momentum of the ejected gas by means of a realistic thermophysical model and by taking into account the nucleus kinematics. By using the change in orbital period as an observable, it is then possible to directly determine the nucleus mass and, if estimates of its size and shape are available, its bulk density. Rickman (1986, 1989) successfully applied this method to estimate the density of 1P/Halley, while Farnham and Cochran (2002) applied it to 19P/Borrelly. Davidsson and Gutierrez (2004, 2005) further refined the method by using the observed change in orbit, the rotational lightcurve, and the observed water production rate as constraints to derive estimates about the size, density and orientation in space of 19P and 67P. It is interesting to note that the densities estimated for 19P by Davidsson and Gutierrez (2004) are somewhat different from those determined by Farnham and Cochran (2002), which shows that those determinations significantly depend on the model assumptions. On the other hand, it is fair to state that most determinations of density obtained from orbital nongravitational models point towards cometary nuclei being underdense, a fact confirmed by direct measurements of the mass—and hence bulk density—of 67P by Rosetta.

1.2 Spin Period Changes

In addition to producing nongravitational accelerations that modify a comet's orbit, activity can also change the nucleus rotational state. The combination of asymmetries in the comet's shape and illumination pattern, and in the distribution of active regions, produces net torques that can modify the spin state of the nucleus, by changing its spin rate and possibly exciting forced precession (see Sect. 1.3). Although long postulated (Whipple 1950, 1982), the first evidence of a spin period change for a comet was only detected in 1994 (Mueller and Ferrin 1996) for 10P/Tempel 2.

As of writing, there are seven Jupiter-family comets (JFCs) for which a change in spin period has been detected, while upper limits on the period change have been placed for four further JFCs (Kokotanekova et al. 2018). Analyzing the known period changes, Mueller and Samarasinha (2018) have proposed a correlation between orbit, activity and rate of change of the spin period. Following this correlation, the largest JFC nuclei with radius $R \geq 3$ km exhibit the smallest period changes (typically $\Delta P < 10$ minutes), while significant rotation period changes of ~ 2 hours per orbit (103P, Meech et al. 2011) and > 20 hours (41P, Bodewits et al. 2018) have been detected for the smallest nuclei (Kokotanekova et al. 2018). Gutierrez et al. (2002) have modeled the spin changes of active cometary nuclei by integrating the Euler equations of motion under the influence of NGAs produced by random activity patterns controlled by a simplified thermal model. They used realistic random shapes for the nuclei, and found that, depending on the simulation parameters, the comet was subject to substantial spin-up or spin-down, while the onset of considerable non-principal-axis rotation was rare. They concluded that NGA-induced spin-up can therefore be considered an important mechanism for cometary splitting, as described by Davidsson (1999, 2001). Since both the orbital dynamics and the spin period changes are caused by the same nongravitational acceleration due to sublimation activity, these two properties are expected to

be related. Rafikov (2018) used data for the seven comet nuclei for which changes in the spin rate and orbit have been determined and found a linear relationship between the change of the cometary rotation rate and the magnitude of its NGA.

1.3 Complex Rotation

Reaction torques from outgassing can have two effects on the rotational state of comets. The first one is a change in the direction and magnitude of the angular momentum vector. The second one is the possible onset of non-principal-axis (hereafter NPA) rotation (sometimes called "excited" or "complex" rotation in the literature). Assuming that a cometary nucleus is a rigid body, its dynamics are controlled by Euler's equations of motion, in which the ratios of the moments of inertia determine the different periods involved in the complex rotational motion of the nucleus. A thorough characterization of the rotational state of a nucleus can thus provide valuable information on its moments of inertia, which, in conjunction with the knowledge of its shape and mass, can be diagnostic of its internal mass distribution. Eventually, energy dissipation due to internal friction resulting from mechanical deformation of the nucleus, can lead to the relaxation of the NPA rotation down to the minimum energy level: a pure rotation around the axis of maximum moment of inertia. Monitoring the evolution of the excited rotation with time can therefore place constraints on the relaxation time of NPA rotation, which in turn can provide information on the mechanical properties of the nucleus (Samarasinha et al. 2011).

Two NPA modes can appear depending on the rotational energy level: *short-axis modes* (SAM) and *long-axis modes* (LAM, see Samarasinha and A'Hearn 1991). Timescales and equations are described in detail in Sect. 2 of the review on comet rotation by Samarasinha et al. (2004). Such complex NPA rotational states have been invoked in the past to reconcile lightcurves and imaging data of comet 1P/Halley (Belton 1991; Samarasinha and A'Hearn 1991), to explain the lightcurves of comets 2P/Encke (Belton et al. 2005) and possibly 29P/Schwassmann-Wachmann 1 (Meech et al. 1993), and to interpret the CN jets, spacecraft imaging and radar data of comet 103P/Hartley 2 (Samarasinha et al. 2011; Waniak et al. 2012; Belton et al. 2013). More recently, NPA rotation has been proposed to explain the lightcurves and morphology of comet 252P/2000 G1 LINEAR (Li et al. 2017) and of the interstellar object 1I/2017 U1 'Oumuamua (Belton et al. 2018).

1.4 Comet Splitting

Over the past two centuries, more than 40 comets have been observed to split into two or more components (Boehnhardt 2004) with a rate of $\sim 10^{-2}$ yr^{-1} per nucleus (Chen and Jewitt 1994). One splitting mechanism is represented by tidal forces occurring when a nucleus experiences an encounter with a massive object. A notable case was comet Shoemaker-Levy 9, that split in a string of fragments in July 1992 as a consequence of a close encounter with Jupiter (Solem 1994).

Possible disintegration mechanisms for non-tidally split nuclei are the build-up of mechanical stresses due either to large temperature/pressure gradients on the nucleus or to the centrifugal pull as a consequence of fast rotation (Sekanina 1997; Boehnhardt 2004). Nucleus spin-up due to nongravitational acceleration therefore represents one viable mechanisms leading to comet splitting. In this scenario, if a comet spins up and reaches an instability limit, where the centrifugal force exceeds self-gravity and the material forces, the comet nucleus starts to shed mass and disintegrates. Davidsson (1999, 2001) developed analytical models to study the critical breakup spin rate as well as the splitting behavior of solid

nuclei with spherical and ellipsoidal shapes. These models describe well the observed JFC population and have been used to study the tensile strength of JFCs (Kokotanekova et al. 2017; Toth and Lisse 2006; see also Groussin et al. 2019, in this issue).

2 Available Constraints for 67P

2.1 Orbital Evolution

The orbital parameters of 67P, including the Marsden A_{ng} terms introduced above, have been derived from ground-based observations and are available for each of its previous apparitions.

From August 2014 to September 2016, 67P was accompanied in its orbit by the Rosetta spacecraft, allowing high accuracy astrometry to be conducted. This was achieved through radio-tracking of the spacecraft combined with optical navigation, which allowed an accurate measurement of the location of the nucleus relative to Rosetta, by using the navigation camera and the OSIRIS instrument (Optical, Spectroscopic, and Infrared Remote Imaging System; Keller et al. 2007). The combined positioning allowed the ESA flight dynamics team to produce a model of the comet's trajectory, available as NASA SPICE kernels (Acton 1996), with a theoretical accuracy of ∼10 m in the Earth-comet range direction and better than ∼100 km in the perpendicular (across-track) direction (Godard et al. 2015, 2017). Unfortunately, as of the time of writing, the flight dynamics reconstruction is a purely gravitational solution, i.e. it does not include a nongravitational force model and deals with the resulting drift by "resetting" the modeled trajectory with the observed comet position at the beginning of each of the segments of the integration. Attree et al. (2019) showed that this resetting is convolved with the initial positional uncertainty in each segment and therefore manifests as a series of random "jumps" in the SPICE trajectory at intervals ranging from 3–4 days during perihelion, to ∼1 month during other phases of the mission.

As can be seen in Fig. 1, the discontinuities limit the accuracy of the reconstructed trajectory to between tens to over a hundred kilometers in three-dimensional heliocentric position, but are generally smaller than 1 km in the Earth-comet range direction.

The reconstructed trajectory still represents a gravitational solution plus the effects of the NGAs; theoretically, therefore, a gravitational integration could be subtracted from the SPICE positions and the residuals differentiated twice to obtain the accelerations. However, the discontinuities pose a problem for this differentiation. Two recent papers address this issue in two different ways. Attree et al. (2019) choose to model the NGAs with a full thermal/dynamics model (see Sect. 3, below) and fit the resulting trajectories to the relatively smooth Earth-comet range data. Kramer and Läuter (2019) instead, match the Marsden model to the SPICE positions before fitting the residuals with a series of exponential and polynomial functions up to fourth order. This provides a smooth, differentiable curve from which the NGAs can then be extracted (see Fig. 2). In order to determine the best initial conditions for the orbital integration, they iteratively varied the initial positions and velocities to minimize the residuals to the SPICE positions during a period—400 to 200 days before perihelion—during which the nongravitational acceleration was supposedly negligible. The determined NGAs, along with the SPICE positions themselves when considering the jump uncertainty, are the astrometry constraints to which the NGA models described below can be fitted.

Kramer and Läuter (2019) did not incorporate a thermophysical model of the cometary activity in their model, and therefore could not independently estimate gas production from
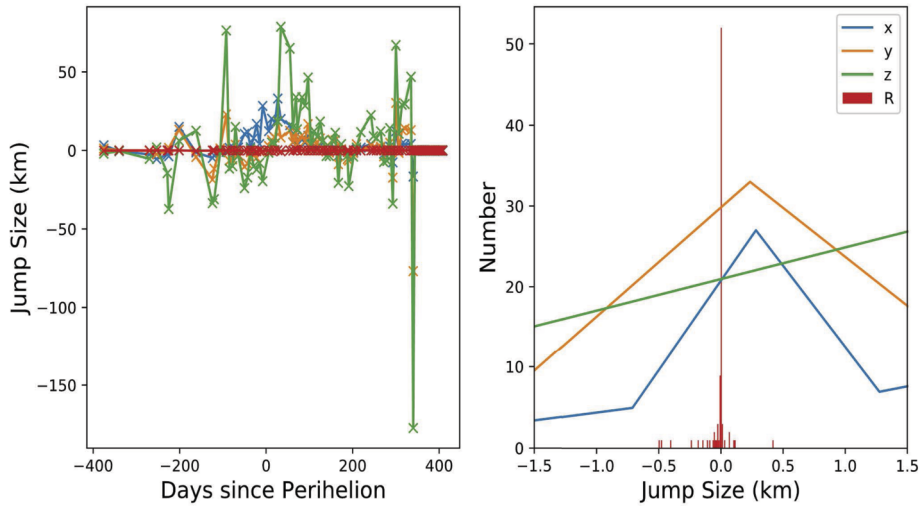
Fig. 1 Discontinuities in the position of comet 67P from the SPICE kernels, in (x, y, z) heliocentric J2000 coordinates, and Earth-comet range (R), from Attree et al. (2019). On the left, discontinuities are shown as a function of time and on the right as a histogram of jump sizes

Fig. 2 The three components of the nongravitational acceleration in the terrestrial equatorial frame after Kramer and Läuter (2019). The shaded areas correspond to the error envelope obtained by perturbing the initial conditions of the orbital integration
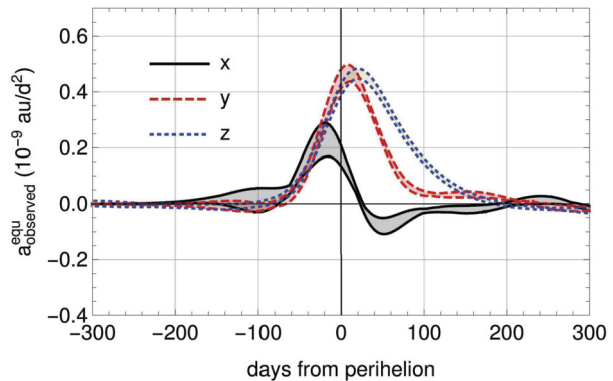
the NGAs. However, by studying the direction of the reaction force, they infer the presence of a diurnal lag in the direction of the NGAs with respect to the antisolar direction, up to 50° in the period between perihelion and 140 days post perihelion.

2.2 Spin Rate and Rotation State

Pre-Rosetta observations of 67P with the aim of determining the spin period were all performed between (and far from) the perihelion passages of Sep. 2002 and Feb. 2009. Lowry et al. (2012) used the best observational base available at that time to determine a rotation period $P = 12.76137 \pm 0.00006$ h. When Rosetta started the approach to the still unresolved 67P, in early 2014, it immediately became clear from OSIRIS disk-integrated lightcurves that the rotation period had changed to $P = 12.4043 \pm 0.0007$ h after the 2009 perihelion passage (Mottola et al. 2014). This was the first evidence that the rotation of 67P was strongly affected by nongravitational torques.

Prompted by this finding, Keller et al. (2015b) performed forward modeling of the nucleus kinematics subjected to sublimation torques, to predict the spin evolution around the 2015 perihelion passage. For this purpose they used a detailed (although preliminary) comet digital shape model (Preusker et al. 2015) and a two-layer thermophysical model (Keller et al. 2015a). The model correctly predicted that the comet would start to slow down its rotation shortly prior to the 2015 perihelion, and would rapidly spin up around perihelion. This study also highlighted the importance of a realistic thermal model and of a detailed shape model of the target for the description of the spin evolution, since both strongly affect the net torques.

The Rosetta mission also offered a unique opportunity to accurately monitor the rotational parameters of 67P with a high accuracy throughout the perihelion passage, and to search for possible NPA rotation. First hints of a complex rotation were indeed identified at the beginning of the mission during the stereophotogrammetric reconstruction of the nucleus shape (Preusker et al. 2015). Later, a periodogram analysis of the (RA, Dec) direction of the instantaneous angular velocity and nucleus Z-axis vectors provided by landmarks tracking data confirmed a slight NPA rotation (Jorda et al. 2016). Both data sets were compatible with a small amplitude SAM (0.15°), very close to the pure spin state of minimum energy. The period associated to this modulation was found to be close to 270 h in both cases. In an attempt to explain the observed NPA rotation, Gutierrez et al. (2016) tried to reproduce the data of Jorda et al. (2016) with the mathematical formalism of Samarasinha and Mueller (2015) for a torque-free nucleus. Although they could not derive unique ratios for the moments of inertia, they did find that the moments of inertia I_X, I_Y and I_Z are linked by the relationship: $I_Z \approx 0.96 I_X + 0.99 I_Y$.

2.3 Splitting

Hirabayashi et al. (2016) performed a Monte Carlo study of the orbital and spin evolution of 67P by integrating 1000 clones backwards in time for a period of 5000 years and simulating sublimation-induced torques. They found that the spin rate variation becomes completely random within the integration period, and that the period inverts its rate of variation several times in a random-walk way. They also found that when the spin exceeded the fission limit of ∼7 h, the two lobes composing the comet become temporally co-orbiting. Such a configuration, however, is short lived, after which the two bodies coalesce again into a re-configured body. The authors argue that 67P may have undergone several such reconfiguration phases since its formation, and that some of the large features visible today on the comet might be previous contact points between the two lobes, now exposed due to this rearrangement.

Further, by means of an elastic and plastic finite-element model, they interpret the presence of a long crack in the comet's Hapi region as the effect of tensile stresses during the phase in which the comet nearly reached—but did not exceed—the fission limit. The authors also argue that such evolution could be typical for most bilobate comets, whereas single bodies could either be primordial objects or surviving components of a pair.

2.4 Gas Production, Dust Production, Mass Loss

Because NGA is produced by the reaction force induced by the exchange of momentum between the comet and the ejected gas and dust, it is important to estimate the gas production, dust production and mass loss of 67P.

2.4.1 Water Production

The water production rate from 67P had been measured during pre-Rosetta apparitions in 1982/83 (Hanner et al. 1985; A'Hearn et al. 1995; Crovisier et al. 2002; Feldman et al. 2004; Schleicher 2006), 1995/6 (Schleicher 2006; Bertaux et al. 2014), 2002 (Bertaux et al. 2014) and 2008/9 (Ootsubo et al. 2012; Snodgrass et al. 2013; Bertaux et al. 2014). Some of these measurements were performed only at a given time and heliocentric distance, but some tracked the change in production rate around perihelion. Most of these estimates agree on a maximum production rate around perihelion of about 10^{28} s^{-1}.

The Rosetta mission presented an opportunity to track the changes in water production in unprecedented detail for a long period of time and with a variety of different instruments. Some of the first measurements from MIRO (Microwave Instrument for the Rosetta Orbiter) estimated the water production from the nucleus between June and September 2014. Gulkis et al. (2015) reported the first estimate of 1×10^{25} s^{-1} at 3.9 au in June and then a higher value of 4×10^{25} s^{-1} in August at 3.5 au. Lee et al. (2015) looked in greater detail at the spectral lines measured in August 2014 and estimated water production rates varying by a factor 30, from 0.1×10^{25} to 3×10^{25} s^{-1}. The authors attributed such a large variation in water production to a non-uniform distribution of sublimating water ice over the comet's surface.

Later, in September at 3.4 au, the production rate of the main water isotopologue ($H_2^{16}O$) was derived as $(4.9 \pm 2.5) \times 10^{25}$ s^{-1} (Biver et al. 2015). Further values for the water production were derived from observations by ROSINA (Rosetta Orbiter Spectrometer for Ion and Neutral Analysis). Between August and November 2014 (3.5 to 3.0 au), the ROSINA-COPS (Pressure Sensor) estimated the production as 8.7×10^{25}–1.1×10^{26} s^{-1}, and then between November and January 2015 (3.0 to 2.5 au), the water outgassing rate was a factor of two higher (Bieler et al. 2015). From ROSINA-DFMS (Double Focussing Mass Spectrometer), Fougere et al. (2016) estimated the change in water production on approach to perihelion, finding that it increased from $< 10^{26}$ s^{-1} at 3.5 au, to $> 10^{27}$ s^{-1} at 1.5 au. Estimates on the water production rate in this time period were also made by Bockelee-Morvan (2015) using VIRTIS-H (Visible and Infrared Thermal Imaging Spectrometer). From November 2014 to January 2015 (2.9–2.5 au), the outgassing rate was between 6.9×10^{25} and 8.7×10^{25} s^{-1}. Together, these measurements show that the water outgassing was approximately 10^{26} s^{-1} at the end of 2014 and beginning of 2015.

Fink et al. (2016) analyzed data cubes from VIRTIS-M measured in February 2015 (2.21 au) and April 2015 (1.76 au) and found water production rates of 2.5×10^{26} and 4.65×10^{26} s^{-1}, respectively. They also examined the spatial distribution of outgassing in these observations, deriving that 83% of the water production comes from the illuminated side and 17% from the night side. In addition, the highly active neck region was found to contribute about 60% to the water production from an observation in February 2015. For comparison, in April 2015, Migliorini et al. (2016) found a higher estimate for the water outgassing of 10^{27} s^{-1} using measurements made by VIRTIS-M. Using the RPC-ICA (Rosetta Plasma Consortium Ion Composition Analyser), Simon Wedlund et al. (2016) estimated the change in water production rate to be 2×10^{25} s^{-1} in September 2014 to 5×10^{26} s^{-1} in April 2015.

The long-term evolution of the water production rate has also been assessed. Hansen et al. (2016) and Marshall et al. (2017) measured the water production rate from August 2014 to April 2016 with the ROSINA and MIRO instruments, respectively, and Läuter et al. (2019) assessed the water production up to September 2016. The maximum water production rates were found to be $(3.5 \pm 0.5) \times 10^{28}$ s^{-1} (Hansen et al. 2016), $(1.4 \pm 0.5) \times 10^{28}$ s^{-1} (Marshall et al. 2017) and $(2.0 \pm 0.1) \times 10^{28}$ s^{-1} (Läuter et al. 2019). The measurements from ROSINA produced slightly larger results than those from MIRO, and although a satisfactory explanation for this discrepancy is still not established, it might result from the basic difference
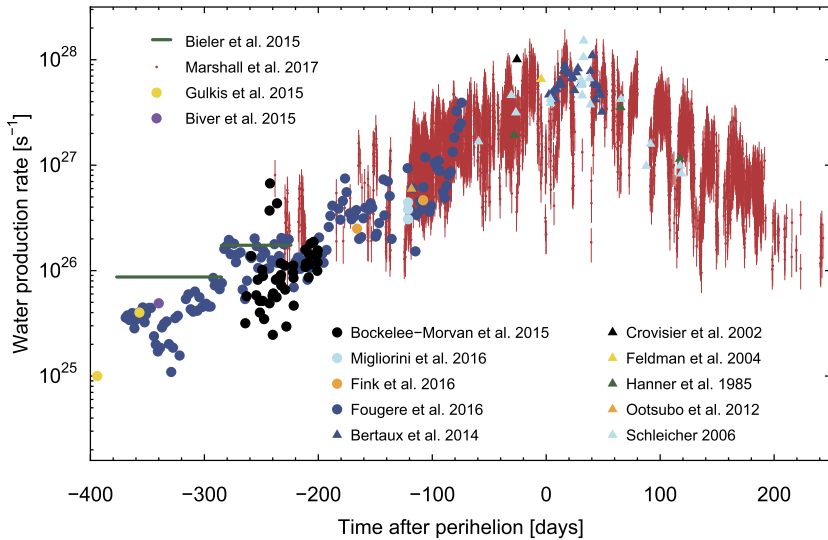
Fig. 3 Water production rates for 67P calculated from Rosetta and ground-based measurements. Adapted from Marshall et al. (2017)

between the two instruments. ROSINA, being an *in situ* instrument, measures the gas density in the local vicinity of the spacecraft. MIRO—a remote-sensing instrument—measures the column density along the line of sight. The discrepancy may arise from different acquisition techniques and inversion models required to retrieve the gas densities.

The Rosetta measurements generally confirm the prior measurements for the water production, finding that the maximum production around perihelion is $> 10^{28}$ s^{-1} and that the maximum production is shifted after perihelion. Additionally, the results indicate that there is an asymmetry in the outgassing pre- and post-perihelion (Hansen et al. 2016; Läuter et al. 2019). The production rate as a function of the heliocentric distance can be roughly approximated as a power law. The exponent of the power law has been measured by several authors: -7.06 (Simon Wedlund et al. 2016), -5.1 (Hansen et al. 2016), -3.8 (Marshall et al. 2017) and -7 (Läuter et al. 2019) pre-perihelion; and -7.15 (Hansen et al. 2016), -4.3 (Marshall et al. 2017) and -6.5 (Läuter et al. 2019) post-perihelion. As noted by (Marshall et al. 2019), these values must be treated with caution, though, as the power law exponent is in general not constant, but is also a function of heliocentric distance.

Läuter et al. (2019) attempted to determine the spatial distribution of the water production. Although the exact location of the active regions is not unique, generally the water production follows the seasonal illumination, originating from the Northern side far from perihelion and shifting to the Southern side at perihelion. The outgassing appears to follow the sub-solar point as it moves from North to South and then back to the Northern side on the outbound leg. This trend is also seen in the regional analysis by Marshall et al. (2017). The results of Fougere et al. (2016) and Hansen et al. (2016) point to a slightly more complicated picture: they find active regions in the Northern neck region and on the Southern lobe, and when these regions are well illuminated, they contribute significantly to the outgassing, but when they are not so well illuminated, water production is more uniformly distributed around the comet surface. The water production rates for 67P are summarized in Table 1 and Fig. 3.

Table 1 Summary of production rates and mass loss from 67P during the 2015 apparition

	2.2 au pre-perihelion production	Perihelion production	Total mass loss (kg)
H_2O	2.5×10^{26} s^{-1} (6)	$(3.5 \pm 0.5) \times 10^{28}$ s^{-1} (1) $(1.42 \pm 0.51) \times 10^{28}$ s^{-1} (2) $(2.0 \pm 0.1) \times 10^{28}$ s^{-1} (5)	6.4×10^9 (1) $(2.4 \pm 1.1) \times 10^9$ (2)
CO_2	1.18×10^{25} s^{-1} (6)	10^{27} s^{-1} (5)	
Dust	(60 ± 10) kg s^{-1} (4)	$(1.7 \pm 0.9) \times 10^4$ kg s^{-1} (4)	
All material			4–8×10^{10} (1) $(1.2 \pm 0.6) \times 10^{10}$ (2) $(1.05 \pm 0.34) \times 10^{10}$ (3)

(1) Hansen et al. (2016); (2) Marshall et al. (2017); (3) Pätzold et al. (2019); (4) Fulle et al. (2016); (5) Läuter et al. (2019); (6) Fink et al. (2016)

2.4.2 Other Species

The production rates for other species have also been measured. For CO_2, Fink et al. (2016) estimated production rates in February 2015 and April 2015 of 1.18×10^{25} and 1.13×10^{25} s^{-1}, at 2.21 au and 1.76 au, respectively. In comparison to water, which shows a fairly predictable outgassing correlating to illumination, CO_2 in this work appeared to originate in isolated regions or spots. As a result of different outgassing behavior, it is difficult to interpret local measures in terms of CO_2/H_2O ratios.

In April 2015, VIRTIS-M measurements implied an enhanced production rate of CO_2—8×10^{25} s^{-1} at 1.9 au (Migliorini et al. 2016). In addition to water (described above) Läuter et al. (2019) also estimated the production of CO_2, CO and O_2, from DFMS/COPS data. These molecules peaked at perihelion with production rates of 10^{27} s^{-1} (CO_2), 5×10^{26} s^{-1} (CO) and 3×10^{26} s^{-1} (O_2). All of these molecules are less abundant than water (1–10%), however their results indicate that on the outbound leg, beyond 3 au, it is possible that water in the coma becomes less abundant than CO_2 and even CO. The O_2 production is similar to H_2O in that it shifts from North to South during perihelion passage but CO_2 and CO appear to be consistently originating from the Southern hemisphere, regardless of heliocentric distance.

Bockelee-Morvan (2015) estimated the change in abundance of CO_2, CH_4 and OCS for a few tens of days around perihelion from spectral observations made by VIRTIS-H. Relative to water, CH_4 and OCS have abundances of 0.23% and 0.12%, respectively, pre-perihelion, and 0.47% and 0.18% post-perihelion. CO_2 has an abundance of 14% pre-perihelion and then increases substantially post-perihelion to 32%. The maximum increase in CO_2 has a lag of 6 days, which compares to the behavior to water which also experienced peak production 20 days after perihelion. With ROSINA DFMS measurements made in May 2016, Rubin et al. (2018) measured the abundance of a number of minor species in the coma of 67P. Here, production rate ratios relative to water are reported (all in s^{-1}): $(8.9 \pm 2.4) \times 10^{-4}$ (N_2), $(4.9 \pm 1.9) \times 10^{-6}$ (^{36}A), $(5.8 \pm 2.2) \times 10^{-6}$ (Ar), $(4.9 \pm 2.2) \times 10^{-7}$ (Kr), $(2.4 \pm 1.1) \times 10^{-7}$ (Xe) and $< 5 \times 10^{-8}$ (Ne).

Around perihelion, the total gas production rate is about 30% larger than the one due to water production alone. Due to the large uncertainties in the derived water productions, it is generally justified to neglect the contribution of other species to the NGA. However, it

must be considered that a possible different spatial distribution of the source regions of the different species could introduce small systematic deviations when modeling the orbital and spin evolution. Activity beyond 3 au is dominated by supervolatile species. However, the contribution of activity to the total NGA is negligible at these large heliocentric distances.

2.4.3 Dust Production

Several instruments onboard Rosetta have been used to estimate the amount of dust ejected from the surface. Rotundi et al. (2015) measured the dust production in August and September 2014 as the comet moved from 3.6 au to 3.4 au inbound using observations made by GIADA (Grain Impact Analyser and Dust Accumulator) and OSIRIS. They found a distribution for the ejected mass ranging from 10^{-10} to 10^{-2} kg which peaked at 10^{-2} kg with a differential power-law slope of -2 in the lower mass bins.

The mass loss in each mass bin varied from 1.5 kg s^{-1} to 9.9×10^{-3} kg s^{-1}, giving a total mass loss of (7 ± 1) kg s^{-1} for this time period. The combination of GIADA and OSIRIS was used again by Fulle et al. (2016) to derive the dust loss from 2.2 au to 1.2 au (perihelion). This evolved from (60 ± 10) kg s^{-1} at 2.2 au, to (70 ± 30) kg s^{-1} at 2.1 au and finally $(1.7 \pm 0.9) \times 10^4$ kg s^{-1} at perihelion.

By excluding material larger than 1 kg, the mass loss at perihelion would be $(1.5 \pm 0.5) \times 10^3$ kg s^{-1}. This value can be compared to the maximum production of water, (426 ± 153) kg s^{-1} measured by Marshall et al. (2017) at perihelion. The mass distribution reported by Fulle et al. (2016) steepens at perihelion compared to the distribution at larger heliocentric distances.

2.4.4 Mass Loss

Using water production rates from previous apparitions and some early Rosetta results, Bertaux et al. (2015) estimated the mass loss and erosion of material from 67P. The resulting total mass loss over one orbit was $(2.7 \pm 0.4) \times 10^9$ kg from observations performed by SWAN/SOHO, corresponding to an erosion depth of about 1 m.

Between 3.6 au inbound and 3.0 au outbound, Hansen et al. (2016) estimate the total water mass loss to be 6.4×10^9 kg. By making assumptions about the ratios of the minor gas species and the dust-gas ratio, a total mass loss of 4–8×10^{10} kg can be expected.

As stated before, lower values for the water production were estimated from MIRO observations. As a consequence, Marshall et al. (2017) also estimate a lower value for the mass loss, $(2.4 \pm 1.1) \times 10^9$ kg for water loss and $(1.2 \pm 0.6) \times 10^{10}$ kg for the total mass loss, although they do not account for the mass loss of minor species.

The radio science experiment RSI calculated the mass of 67P as $(9982 \pm 3) \times 10^9$ kg at the start of the Rosetta mission and $(9971.5 \pm 1.5) \times 10^9$ kg at the end of the mission, giving a total mass loss of $(10.5 \pm 3.4) \times 10^9$ kg during this apparition (Pätzold et al. 2019)[1].

Keller et al. (2017) estimate that a mass loss of this magnitude would erode to depths of 0.55 m for a uniformly outgassing, mass-equivalent sphere. This is much less than the theoretically calculated maximum capability of erosion from an ice/dust matrix covered by a thin inert layer, which was found to be 20 m (Keller et al. 2015a). This supports the notion that the active ice fraction (i.e. the fraction of the surface that can contribute to sublimation) must be much smaller than 1. It is worth restating that the total mass loss is only a fraction

[1]Note that in Pätzold et al. (2019) pre- and post-perihelion masses of $(9982 \pm 3) \times 10^{12}$ kg and $(9971.5 \pm 1.5) \times 10^{12}$ kg, respectively, are erroneously reported throughout their paper.
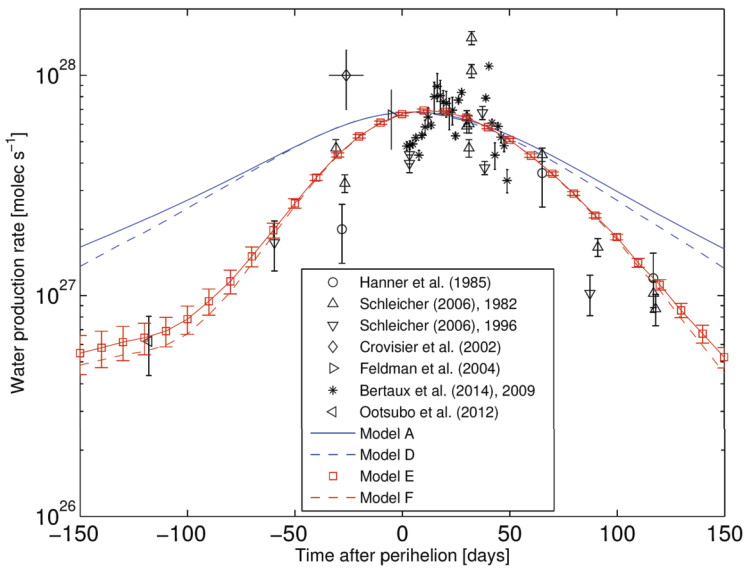
Fig. 4 Observed and modeled water production rates for 67P after Keller et al. (2015a). Their models E and F provided the best fit to the data and were derived by adopting regionally variable activity levels for two different values of thermal inertia, respectively. Models A and D are models with constant properties over the surface. Model A is a simple stationary model with ice at the surface and D is a full thermodynamical model including thermal transport

of the total material that is ejected from the surface as some of the lifted material falls back onto the surface. Mass transport on 67P is described by Keller et al. (2017), with about 20% of the eroded material from the South estimated to fall back onto the Northern side.

3 Modeling Approaches

In addition to bearing interest for the study of orbital and spin evolution, and the occurrence of splitting events, NGAs provide powerful constraints for the determination of the thermophysical properties of the nucleus. The information content of the spin evolution and of the orbital evolution are quite complementary. The nongravitational resultant torque is the sum of the local reaction components, most of which mutually cancel out, with only the asymmetries in the shape, illumination, and activity distribution contributing to the spin evolution. A small change in the distribution of active regions (at constant average total production rate) can cause large changes (even a reversal) of the induced torque. Therefore, the spin evolution is most diagnostic for the spatial distribution of activity. Conversely, the orbital evolution is more diagnostic of the total production rate. Once the NGAs can be reliably retrieved from observations, they can therefore provide independent constraints for the thermophysics of cometary activity and its distribution on the nucleus.

One of the conclusions of the thermophysical modeling by Keller et al. (2015a) was that no *bona fide* thermal model that uses constant physical properties—over time and over the surface of the comet—can accurately reproduce the observed water production rate as a function of heliocentric distance, as measured by the Rosetta analyzers. Keller et al. (2015a) also showed that an *ad hoc* distribution of active ice fraction over the body could explain the observed results, even though it does not represent a unique solution (see Fig. 4).

However, the peculiarity of the 67P orbit and pole orientation—with its Southern solstice occurring close to perihelion, and its large obliquity—creates a strong coupling between sub-solar latitude and heliocentric distance. As a consequence, the observed water production as a function of heliocentric range could as well be explained by a regionally uniform comet, whose properties (e.g. dust layer thickness or active fraction) vary with time. Things are complicated by the fact that production rates were measured by Rosetta with different instruments that applied different measurement principles, measured on different spatial and temporal scales and required complex modeling in order for their data to be translated into a flux of molecules. As a result, as could be seen in Sect. 2.4, the measurements from different instruments can be difficult to compare to each other. Ideally, a model aiming to explain the physics of activity should be able to reproduce all of the available measurements of gas production, both on regional and on global scale, as well as its seasonal and secular variations. Using production data alone, however, the models are generally underconstrained, producing ambiguous results. Using in addition the nongravitational effects as constraints holds the potential of disentangling the contributions of a time-varying and regionally-varying activity, as highlighted in the following.

3.1 Regional Activity Modeling

Further to the *ad hoc* distributions of active ice fraction used by Keller et al. (2015a) and Kramer et al. (2019), several authors have attempted to link heterogeneous activity to regional surface variations on the nucleus. For example, in Marschall et al. (2016) and Marschall et al. (2017), the authors fit the pre-perihelion water production rates with a basic thermophysical model by varying local active fractions on the nucleus's cliffs versus its plains, Northern verses Southern hemispheres, and in six geographically grouped regions. Attree et al. (2019) fitted a similar model to the combined trajectory, rotation and production measurements by varying the active fraction in the Marschall et al. (2016, 2017) regions, as well as the 26 named geographical regions of Thomas et al. (2015). Their results, shown in Fig. 5, match the initial slope of production and NGA but break down around perihelion, suggesting temporal variations as discussed below.

The mapped active fraction is relatively consistent across several works (Marschall et al. 2016, 2017; Kramer et al. 2019; Attree et al. 2019) in showing the highest values in the Southern hemisphere, with intermediate values in the deposition regions of the Northern neck (Hapi), and the lowest values elsewhere in the North. The poor torque fit in the combined fit demonstrates that the spatial distribution of "torque efficiency", the propensity for outgassing in a particular area to influence the nucleus rotation, does not necessarily correlate with the geographically defined regions. Significant improvements to the torque fit could be made in Attree et al. (2019) by parametrizing the Southern hemisphere in terms of this torque efficiency, which led to a spotty activity distribution with enhanced peaks in Anhur, Bes, Khepry, and parts of Wosret.

3.2 Time-Dependent Activity Modeling

Attree et al. (2019) did not find adequate solutions to their combined fit to the 67P trajectory, rotation and production measurements with the above parametrization of a spatially varying active fraction. They therefore invoked a time-dependent active fraction, with the active fractions of two regions in the Southern hemisphere allowed to vary between two values. Only the Southern regions were varied in this way, as the discrepancies between the
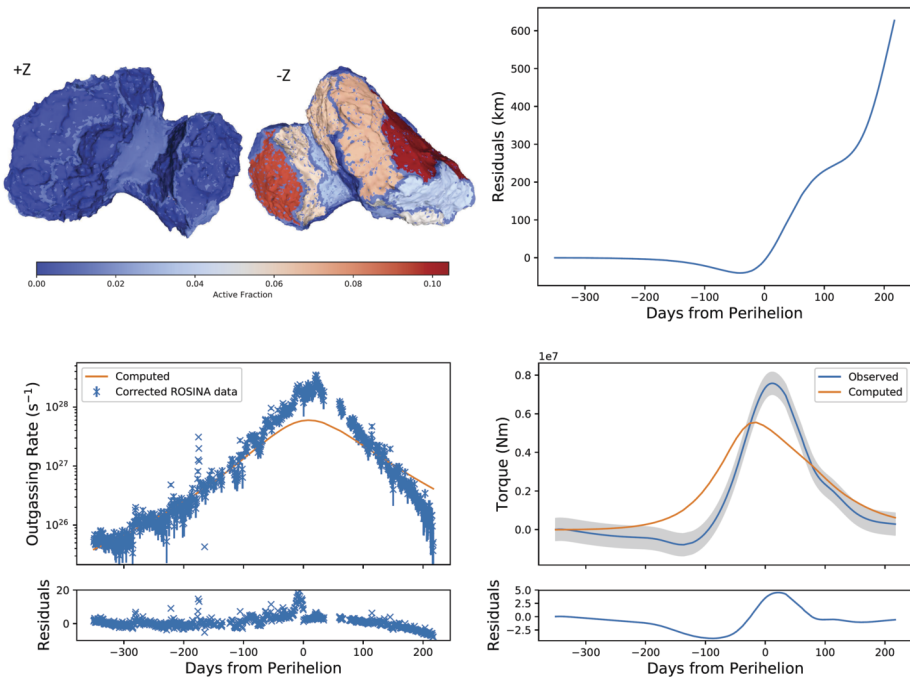
Fig. 5 The best-fit solution of a thermophysical model from Attree et al. (2019) with varying active fractions in the 26 named comet regions (their solution B). Top left: Active fraction mapped onto the comet; top right: residuals in Earth-comet range relative to the SPICE solution; bottom left: total gas production relative to ROSINA; bottom right: torque relative to OSIRIS measurements

observations and time-independent models were greatest around perihelion, when the South dominates activity.

Attree et al. (2019) found good solutions, with significant improvement over time-independent models, by drastically increasing the Southern active fraction (from around 10% to 25–35%) in the ~hundred days around and just after perihelion (see Fig. 6). This allowed production to ramp-up to meet the high observed perihelion activity (right of Fig. 6) before falling off quickly again as seen by ROSINA.

The trajectory fit was likewise improved over a time-independent model, supporting the idea of a steeper slope of the activity at perihelion than at larger heliocentric distances, in agreement with the observed water production curve.

The interpretation for the cause of such a time-varying active fraction is that of changes and movement in surface dust cover. As has been suggested by several authors (e.g. Fornasier et al. 2016), strong activity lifts dust at perihelion with greater efficiency, exposing more volatile-enriched material and increasing the sublimation rate in a positive feedback. Dust would then be ejected or transported, mainly to the Northern hemisphere (Lai et al. 2016; Keller et al. 2017), before the decreasing activity post-perihelion allows it to once again be deposited in the South. Gas fluxes through a thicker dust mantle are then quenched, reducing the effective active fraction again.

Time-dependent activity is also implied by Kramer et al. (2019). In fitting the rotation rate, spin-pole direction and total gas production, they use a time-constant effective active fraction (fitting for both a spatially uniform fraction, and one varying in patches), but note
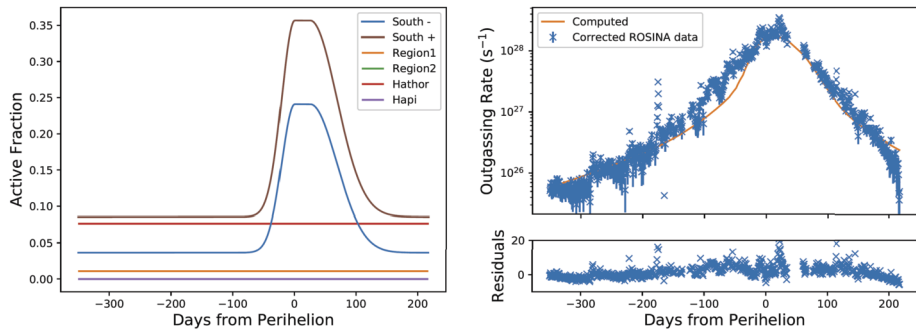
Fig. 6 Best-fit time-dependent model of Attree et al. (2019) (their model C). Left: the active fractions of their six super regions with time. Right: the resulting fit and residuals to the total production rate, showing a marked improvement over the time-independent models of above. The active fraction for the Southern hemisphere is reported separately for regions that contribute to increase or decrease the spin rate, indicated with a plus and minus sign in the legend, respectively

that the gas production in particular can only be matched with an effective sublimation curve with an "enhanced response near perihelion", above the standard energy balance solution. Kramer et al. (2019) suggest the same thinning and thickening of a surface dust layer to explain this curve, citing the two thermal models of Keller et al. (2015a), who modeled the effects of different dust layer thicknesses on sublimation rates.

They raise the possibility of a mixed model that transitions between the two thermal regimes as the comet approaches the sun. Given the difficulty found in trying to fit time-independent models to the Rosetta data, this seems like a promising direction for future work.

It should be noted that, as discussed in Kramer and Läuter (2019), the nongravitational torques place the most stringent constraint on the spatial distribution of activity, whereas the accelerations and total production place more constraints on the temporal variability. Time-dependent activity appears necessary to reproduce not just the high peak activity seen at perihelion but also the quick falloff with heliocentric distance afterwards (i.e. simply having large active fractions in the South alone cannot match observations), while simultaneously improving the trajectory fit.

3.3 Thermophysics of Activity

For the purpose of understanding nongravitational forces, the variation of gas production of a comet as a function of heliocentric distance is of paramount importance. The close relationship between macroscopic characteristics and details of microphysical processes and/or properties of the cometary nucleus is nontrivial. While the overall picture of cometary activity, as outlined by Whipple (1950) is still valid today, the details are far from being understood.

Today it is clear that modern theoretical models aiming to describe cometary activity should explicitly take into account the fact that volatile sublimation does not occur at the surface of the nucleus, but takes place under a porous dusty crust. Such models were proposed in Keller et al. (2015a), Skorov et al. (2016), Hu et al. (2017a,b). The dust particles forming this crust have a complex chemical (Bardyn et al. 2017) and morphological structure (Langevin et al. 2016; Bentley et al. 2016). When vapor diffuses through a porous layer, a dramatic change in all its characteristics occurs. First, the effective rate of sublimation

depends on the permeability of the layer, controlled by its thickness and pore size (Skorov et al. 2011; Gundlach et al. 2011). Secondly, the surface layer is an extremely non-isothermal region—during day-time, the temperature on the nucleus surface can exceed the temperature of sublimating ice by more than a hundred kelvins on centimeter scales. As a consequence, the sublimating gas is heated up when passing through the dust layer, which leads to the thermal velocity of the ejected molecules being noticeably higher than the kinetic velocity corresponding to the ice temperature. Finally, during diffusion, the angular distribution of the velocity of the escaping molecules may change (Skorov and Rickman 1995). The last two effects clearly affect the reactive force created by the sublimation products, and the resulting nongravitational perturbations. Elementary estimates show that ignoring these processes can lead to a relative error in the estimation of nongravitational forces of the order of 100%.

Nevertheless, this error is much smaller than the possible error caused by the fact that we know very little about the structure of the surface dust layer, and therefore its quenching effect. In all published theoretical models, without exception, it is assumed that the heat transport properties remain unchanged both as the heliocentric distance changes and for different regions of the nuclear surface.

This basic model assumption calls for an upper layer in a stationary state, in which dust particles on the upper boundary of the layer are constantly carried away (ablated) by the gas flow, and exactly replenished by the addition of new particles from the lower boundary of the layer.

Although it seems obvious that this assumption is artificial and non-physical, as of today, no models are available that are more adequate. It is not surprising, therefore, that none of the models mentioned can explain two very important effects we observe on 67P: the steep increase in gas production near perihelion and a delay in maximum gas production with respect to perihelion (see e.g. Hansen et al. 2016). Although in principle seasonal effects could contribute to the latter phenomenon, Keller et al. (2015a) have shown that the equatorial obliquity alone cannot account for the large delay of 20 days observed for 67P in the maximum of the activity.

On the other hand, it was shown above that these effects can be explained by the hypothesis of variability (either spatial or temporal) in activity (see Sect. 3). This concept was proposed for the analysis of observations at the beginning of the mission (Keller et al. 2015a) and was substantiated in Marshall et al. (2019).

Unfortunately, in the form in which it is proposed today, this hypothesis is essentially treated as model parametrization and does not contain a consistent microphysical model describing the observed changes. Nevertheless, it gives us important clues and constraints about what microphysical processes should be included in future models.

4 Conclusions

The long-term observations of 67P by Rosetta covering the onset, progression, maximum, and decay of activity—mainly measured by the varying gas (water) production rates, but also by the observed dust activity—provide a unique chain of results. The novel aspect of the mission is that these coma observations can be combined for the first time with a very detailed shape model of the nucleus. In addition, the magnitude and direction of the instantaneous spin vector and their subtle changes during the perihelion passage are well documented. Thermophysical modeling (Keller et al. 2015a) has shown that no spatially-uniform and time-constant activity model can explain the observed water production rates—especially

the steep increase with decreasing heliocentric distance. Recent work (Fougere et al. 2016; Marschall et al. 2016, 2017; Marshall et al. 2019) has shown that this discrepancy can be reconciled by allowing for spatial and/or temporal variation of the physical properties of the comet's surface in the form of a variable active fraction. The resulting activity distribution patterns, however, are not unique.

Cometary activity is not only reflected in the properties of the resulting coma but also affects the NGA. The NGA induces torques that modify the spin state and an orbital acceleration of the whole nucleus that influences its orbit evolution. Modeling the effects of the NGA provides additional, complementary constraints for the parameters that describe the physics of activity and the spatial and temporal variation of the active fraction. First results have been very recently obtained in this direction by including the effects of NGA (Attree et al. 2019; Kramer et al. 2019; Kramer and Läuter 2019). However, the field is still in its infancy, with the active fraction being incorporated in the models as a pure fitting parameter, disconnected from the physics of activity. The next step will be to incorporate a more realistic model of the physics of activity, including dust removal and transport, which accounts for the observed variability. Further, the use of orbital data currently is limited by the accuracy of the orbit determination of 67P (Attree et al. 2019). It is therefore important that an effort be made in reconstructing the orbit of 67P to the full accuracy that the radio tracking data potentially allow, possibly by including an improved NGA model based on the activity measurements by Rosetta. In this way it will be possible to fully exploit the wealth of data returned by the mission.

References

C.H. Acton, Ancillary data services of NASA's navigation and ancillary information facility. Planet. Space Sci. **44**(1), 65 (1996)

M. A'Hearn et al., The ensemble properties of comets: results from narrowband photometry of 85 comets, 1976–1992. Icarus **118**(2), 223 (1995)

N. Attree et al., Constraining models of activity on comet 67P/Churyumov-Gerasimenko with Rosetta trajectory, rotation, and water production measurements. Astron. Astrophys. **630**, A18 (2019)

A. Bardyn et al., Carbon-rich dust in comet 67P/Churyumov-Gerasimenko measured by COSIMA/Rosetta. Mon. Not. R. Astron. Soc. **469**(S2), 712 (2017)

M.J.S. Belton, Observational and dynamical constraints on the rotation of Comet P/Halley. Icarus **93**, 183 (1991)

M.J.S. Belton et al., The excited spin state of Comet 2P/Encke. Icarus **175**, 181 (2005)

M.J.S. Belton et al., The complex spin state of 103P/Hartley 2: kinematics and orientation in space. Icarus **222**(2), 595 (2013)

M.J.S. Belton et al., The excited spin state of 1I/2017 U1 'Oumuamua. Astrophys. J. **856**(2), L21 (2018)

M.S. Bentley et al., Aggregate dust particles at comet 67P/Churyumov-Gerasimenko. Nature **537**(7618), 73 (2016)

J.-L. Bertaux et al., The water production rate of Rosetta target Comet 67P/Churyumov-Gerasimenko near perihelion in 1996, 2002 and 2009 from Lyman α observations with SWAN/SOHO. Planet. Space Sci. **91**, 14 (2014)

J.-L. Bertaux et al., Estimate of the erosion rate from H_2O mass-loss measurements from SWAN/SOHO in previous perihelions of comet 67P/Churyumov-Gerasimenko and connection with observed rotation rate variations. Astron. Astrophys. **583**, A38 (2015)

F.W. Bessel, Astron. Nachr. **13**, 3 (1835)

A. Bieler et al., Comparison of 3D kinetic and hydrodynamic models to ROSINA-COPS measurements of the neutral coma of 67P/Churyumov-Gerasimenko. Astron. Astrophys. **583**, A7 (2015)

N. Biver et al., Distribution of water around the nucleus of comet 67P/Churyumov-Gerasimenko at 3.4 au from the Sun as seen by the MIRO instrument on Rosetta. Astron. Astrophys. **583**, A3 (2015)

D. Bockelee-Morvan, First observations of H_2O and CO_2 vapor in comet 67P/Churyumov-Gerasimenko made by VIRTIS onboard Rosetta. Astron. Astrophys. **583**, A6 (2015)

D. Bodewits et al., A rapid decrease in the rotation rate of comet 41P/Tuttle-Giacobini-Kresak. Nature **553**, 186 (2018)

H. Boehnhardt, Split comets, in *Comets II* (University of Arizona Press, Tucson, 2004)

J. Chen, D. Jewitt, On the rate at which comets split. Icarus **108**(2), 265 (1994)

J. Crovisier et al., Observations at Nancay of the OH 18-cm lines in comets. The data base. Observations made from 1982 to 1999. Astron. Astrophys. **393**, 1053 (2002)

B.J.R. Davidsson, Tidal splitting and rotational breakup of solid spheres. Icarus **142**(2), 525 (1999)

B.J.R. Davidsson, Tidal splitting and rotational breakup of solid biaxial ellipsoids. Icarus **149**(2), 375 (2001)

B.J.R. Davidsson, P.J. Gutierrez, Estimating the nucleus density of Comet 19P/Borrelly. Icarus **168**, 392 (2004)

B.J.R. Davidsson, P.J. Gutierrez, Nucleus properties of Comet 67P/Churyumov-Gerasimenko estimated from non-gravitational force modeling. Icarus **176**, 453 (2005)

J.F. Enke, Fortgesetzte nachricht über den Pons'schen kometen, in *Berliner astronomische Jahrbuch für das jahr 1826* (1823), p. 135

T.L. Farnham, A.L. Cochran, A McDonald observatory study of Comet 19P/Borrelly: placing the deep space 1 observations into a broader context. Icarus **160**, 398 (2002)

P.D. Feldman et al., Observations of Comet 67P/Churyumov-Gerasimenko with the International Ultraviolet Explorer at Perihelion in 1982, in *The New Rosetta Targets* (Springer, Berlin, 2004)

U. Fink et al., Investigation into the disparate origin of CO_2 and H_2O outgassing for Comet 67/P. Icarus **277**, 78 (2016)

S. Fornasier et al., Rosetta's comet 67P/Churyumov-Gerasimenko sheds its dusty mantle to reveal its icy nature. Science **354**(6319), 1566 (2016)

N. Fougere et al., Three-dimensional direct simulation Monte-Carlo modeling of the coma of comet 67P/Churyumov-Gerasimenko observed by the VIRTIS and ROSINA instruments on board Rosetta. Astron. Astrophys. **588**, A134 (2016)

M. Fulle et al., Evolution of the dust size distribution of Comet 67P/Churyumov-Gerasimenko from 2.2 au to Perihelion. Astrophys. J. **821**(1) (2016)

B. Godard et al., Orbit determination of Rosetta around Comet 67P/Churyumov-Gerasimenko, in *International Symposium on Space Flight Dynamics-25th ISSFD* (2015)

B. Godard et al., Multi-arc orbit determination to determine Rosetta trajectory and 67P physical parameters, in *International Symposium on Space Flight Dynamics-26th ISSFD* (2017)

O. Groussin et al., The thermal, mechanical, structural, and dielectric properties of cometary nuclei after Rosetta. Space Sci. Rev. **215**, 29 (2019)

S. Gulkis et al., Subsurface properties and early activity of comet 67P/Churyumov-Gerasimenko. Science **347**(6220), 0709 (2015)

B. Gundlach et al., Outgassing of icy bodies in the Solar System—I. The sublimation of hexagonal water ice through dust layers. Icarus **213**(2), 710 (2011)

P.J. Gutierrez et al., Evolution of the rotational state of irregular cometary nuclei. Earth Moon Planets **90**(1), 239 (2002)

P.J. Gutierrez et al., Possible interpretation of the precession of comet 67P/Churyumov-Gerasimenko. Astron. Astrophys. **590**, A46 (2016)

M.S. Hanner et al., The dust coma of periodic Comet Churyumov-Gerasimenko (1982 VIII). Icarus **64**(1), 11 (1985)

K.C. Hansen et al., Evolution of water production of 67P/Churyumov-Gerasimenko: an empirical model and a multi-instrument study. Mon. Not. R. Astron. Soc. **462**(7607), 491 (2016)

M. Hirabayashi et al., Fission and reconfiguration of bilobate comets as revealed by 67P/Churyumov-Gerasimenko. Nature **534**, 352 (2016)

X. Hu et al., Thermal modelling of water activity on comet 67P/Churyumov-Gerasimenko with global dust mantle and plural dust-to-ice ratio. Mon. Not. R. Astron. Soc. **469**(S2), 295 (2017a)

X. Hu et al., Seasonal erosion and restoration of the dust cover on comet 67P/Churyumov-Gerasimenko as observed by OSIRIS onboard Rosetta. Astron. Astrophys. **604**, A114 (2017b)

L. Jorda et al., The global shape, density and rotation of Comet 67P/Churyumov-Gerasimenko from preperihelion Rosetta/OSIRIS observations. Icarus **277**, 257 (2016)

H.U. Keller et al., OSIRIS the scientific camera system onboard Rosetta. Space Sci. Rev. **128**, 433 (2007)

H.U. Keller et al., Insolation, erosion, and morphology of comet 67P/Churyumov-Gerasimenko. Astron. Astrophys. **583**, A34 (2015a)

H.U. Keller et al., The changing rotation period of comet 67P/Churyumov-Gerasimenko controlled by its activity. Astron. Astrophys. **579**, L5 (2015b)

H.U. Keller et al., Seasonal mass transfer on the nucleus of comet 67P/Chuyumov-Gerasimenko. Mon. Not. R. Astron. Soc. **469**, 357 (2017)

R. Kokotanekova et al., Rotation of cometary nuclei: new light curves and an update of the ensemble properties of Jupiter-family comets. Mon. Not. R. Astron. Soc. **471**(3), 2974 (2017)

R. Kokotanekova et al., Implications of the small spin changes measured for large Jupiter-family comet nuclei. Mon. Not. R. Astron. Soc. **479**, 4665 (2018)

T. Kramer, M. Läuter, Outgassing induced acceleration of comet 67P/Churyumov-Gerasimenko. Astron. Astrophys. **630**, A4 (2019)

T. Kramer et al., Comet 67P/Churyumov-Gerasimenko rotation changes derived from sublimation-induced torques. Astron. Astrophys. **630**, A3 (2019)

I.-L. Lai et al., Gas outflow and dust transport of comet 67P/Churyumov-Gerasimenko. Mon. Not. R. Astron. Soc. **462**, S533 (2016)

Y. Langevin et al., Typology of dust particles collected by the COSIMA mass spectrometer in the inner coma of 67P/Churyumov-Gerasimenko. Icarus **271**, 76 (2016)

M. Läuter et al., Surface localization of gas sources on comet 67P/Churyumov-Gerasimenko based on DFMS/COPS data. Mon. Not. R. Astron. Soc. **483**, 852 (2019)

S. Lee et al., Spatial and diurnal variation of water outgassing on comet 67P/Churyumov-Gerasimenko observed from Rosetta/MIRO in August 2014. Astron. Astrophys. **583**, A5 (2015)

J.-Y. Li et al., The unusual apparition of comet 252P/2000 G1 (LINEAR) and comparison with comet P/2016 BA_{14} (PanSTARRS). Astron. J. **154**(4), 136 (2017)

S. Lowry et al., The nucleus of Comet 67P/Churyumov-Gerasimenko. A new shape model and thermophysical analysis. Astron. Astrophys. **548**, A12 (2012)

R. Marschall et al., Modelling observations of the inner gas and dust coma of comet 67P/Churyumov-Gerasimenko using ROSINA/COPS and OSIRIS data: first results. Astron. Astrophys. **589**, A90 (2016)

R. Marschall et al., Cliffs versus plains: can ROSINA/COPS and OSIRIS data of comet 67P/Churyumov-Gerasimenko in autumn 2014 constrain inhomogeneous outgassing? Astron. Astrophys. **605**, A112 (2017)

B.G. Marsden, Comets and nongravitational forces. II. Astron. J. **74**(5), 720 (1969)

B.G. Marsden et al., Comets and nongravitational forces. V. Astron. J. **78**(2), 211 (1973)

D.W. Marshall et al., Spatially resolved evolution of the local H_2O production rates of comet 67P/Churyumov-Gerasimenko from the MIRO instrument on Rosetta. Astron. Astrophys. **603**, A87 (2017)

D. Marshall et al., Interpretation of heliocentric water production rates of comets. Astron. Astrophys. **623**, A120 (2019)

K.J. Meech et al., Nucleus properties of P/Schwassmann-Wachmann 1. Astron. J. **106**(3), 1222 (1993)

K.J. Meech et al., Epoxy: Comet 103P/Hartley 2 observations from a worldwide campaign. Astrophys. J. **734**(1), L1 (2011)

A. Migliorini et al., Water and carbon dioxide distribution in the 67P/Churyumov-Gerasimenko coma from VIRTIS-M infrared observations. Astron. Astrophys. **589**, A45 (2016)

S. Mottola et al., The rotation state of 67P/Churyumov-Gerasimenko from approach observations with the OSIRIS cameras on Rosetta. Astron. Astrophys. **569**, L2 (2014)

B.E.A. Mueller, I. Ferrin, Change in the rotational period of Comet P/Tempel 2 between the 1988 and 1994 apparitions. Icarus **123**, 463 (1996)

B.E.A. Mueller, N.H. Samarasinha, Further investigation of changes in cometary rotation. Astron. J. **156**(3), 107 (2018)

T. Ootsubo et al., AKARI near-infrared spectroscopic survey for CO_2 in 18 comets. Astrophys. J. **752**(1), 15 (2012)

M. Pätzold et al., The nucleus of comet 67P/Churyumov-Gerasimenko—Part I: The global view—nucleus mass, mass-loss, porosity, and implications. Mon. Not. R. Astron. Soc. **483**, 2337 (2019)

F. Preusker et al., Shape model, reference system definition, and cartographic mapping standards for comet 67P/Churyumov-Gerasimenko. Stereo-photogrammetric analysis of Rosetta/OSIRIS image data. Astron. Astrophys. **583**, A33 (2015)

R.R. Rafikov, Non-Gravitational Forces and Spin Evolution of Comets (2018). arXiv:1809.05133

H. Rickman, in *Comet Nucleus Sample Return*, ed. by O. Melita. ESA, vol. SP-249, Noordwijk (1986)

H. Rickman, The nucleus of comet Halley: surface structure, mean density, gas and dust production. Adv. Space Res. **9**(3), 359 (1989)

H. Rickman et al., Nongravitational effects and the aging of periodic comets. Astron. J. **102**(4), 1446 (1991)

A. Rotundi et al., Dust measurements in the coma of comet 67P/Churyumov-Gerasimenko inbound to the Sun. Science **347**(6220), 03905 (2015)

M. Rubin et al., Krypton isotopes and noble gas abundances in the coma of comet 67P/Churyumov-Gerasimenko. Sci. Adv. **4**, 7 (2018)

N.H. Samarasinha, M.F. A'Hearn, Observational and dynamical constraints on the rotation of Comet P/Halley. Icarus **93**, 194 (1991)

N.H. Samarasinha, B.E.A. Mueller, Component periods of non-principal-axis rotation and their manifestations in the lightcurves of asteroids and bare cometary nuclei. Icarus **248**, 247 (2015)

N. Samarasinha et al., Rotation of cometary nuclei, in *Comets II* (University of Arizona Press, Tucson, 2004)

N.H. Samarasinha et al., Rotation of comet 103P/Hartley 2 from structures in the coma. Astrophys. J. **734**(1), L3 (2011)

D.G. Schleicher, Icarus **181**, 442 (2006)

Z. Sekanina, The problem of split comets revisited. Astron. Astrophys. **318**, L5 (1997)

C. Simon Wedlund et al., The atmosphere of comet 67P/Churyumov-Gerasimenko diagnosed by charge-exchanged solar wind alpha particles. Astron. Astrophys. **587**, A154 (2016)

Y. Skorov, H. Rickman, A kinetic model of gas flow in a porous cometary mantle. Planet. Space Sci. **42**(12), 1587 (1995)

Y. Skorov et al., Activity of comets: gas transport in the near-surface porous layers of a cometary nucleus. Icarus **212**(2), 867 (2011)

Y. Skorov et al., A model of short-lived outbursts on the 67P from fractured terrains. Astron. Astrophys. **593**, A76 (2016)

C. Snodgrass et al., Beginning of activity in 67P/Churyumov-Gerasimenko and predictions for 2014–2015. Astron. Astrophys. **557**, A33 (2013)

J.C. Solem, Density and size of Comet Shoemaker-Levy 9 deduced from a tidal breakup model. Nature **370**(6488), 349 (1994)

N. Thomas et al., The morphological diversity of comet 67P/Churyumov-Gerasimenko. Science **347**(6220), 03905 (2015)

I. Toth, C.M. Lisse, On the rotational breakup of cometary nuclei and centaurs. Icarus **181**(1), 162 (2006)

W. Waniak et al., Rotation-stimulated structures in the CN and C3 comae of comet 103P/Hartley 2 close to the EPOXI encounter. Astron. Astrophys. **543**, A32 (2012)

F.L. Whipple, A comet model. I. The acceleration of Comet Encke. Astrophys. J. **111**, 375 (1950)

F.L. Whipple, The rotation of comet nuclei, in *Comets* (University of Arizona Press, Tucson, 1982)

D.K. Yeomans et al., Cometary orbit determination and nongravitational forces, in *Comets II* (University of Arizona Press, Tucson, 2004)